# Method of improved scatterer size estimation and application to parametric imaging using ultrasound

Michael L. Oelze[a] and William D. O'Brien, Jr.
*Bioacoustic Research Laboratory, Department of Electrical and Computer Engineering, University of Illinois, 405 North Mathews, Urbana, Illinois 61801*

(Received 28 December 2001; revised 24 August 2002; accepted 26 August 2002)

The frequency dependence of RF signals backscattered from random media (tissues) has been used to describe the microstructure of the media. The frequency dependence of the backscattered RF signal is seen in the power spectrum. Estimates of scatterer properties (average scatterer size) from an interrogated medium are made by minimizing the average squared deviation (MASD) between the measured power spectrum and a theoretical power spectrum over an analysis bandwidth. Estimates of the scatterer properties become increasingly inaccurate as the average signal to noise ratio (SNR) over the analysis bandwidth becomes smaller. Some frequency components in the analysis bandwidth of the measured power spectrum will have smaller SNR than other frequency components. The accuracy of estimates can be improved by weighting the frequency components that have the smallest SNR less than the frequencies with the largest SNR in the MASD. A weighting function is devised that minimizes the noise effects on the estimates of the average scatterer sizes. Simulations and phantom experiments are conducted that show the weighting function gives improved estimates in an attenuating medium. The weighting function is applied to parametric images using scatterer size estimates of a rat that had developed a spontaneous mammary tumor.  [DOI: 10.1121/1.1517064]

PACS numbers: 43.80.Qf, 43.80.Vj [FD]

## I. INTRODUCTION

Conventional B-mode images using ultrasound can resolve structures from hundreds of micrometers to centimeters in scale (structures greater than the acoustic wavelength). A conventional B-mode image is made up of several parallel or consecutively spaced axial RF time signals. Each RF time signal is a series of echoes backscattered from structures in the interrogated medium. In a conventional B-mode image, the frequency-dependent information in the RF time signals is not utilized. Instead, the conventional B-mode image relates the envelope of a backscattered RF time signal to a gray-scale image.

The frequency-dependent information in the RF time signal is related to the tissue microstructure (structures less than the acoustic wavelength).[1–13] Parametrizing the microstructure of tissues has been accomplished by modeling the frequency-dependent scattering from tissues. Several researchers have used parameter information about the shape of the spectrum of sound scattered from tissues to classify tissue microstructure and identify disease.[2,9,11–14] Other researchers have been able to estimate the size, shape and internal make-up of scatterers in tissues from models.[3,5–7,9–11]

Parametric images, which combine the estimated parameters or scatterer properties with conventional B-mode images, have been used to assist with clinical diagnosis and classification of tissue state.[6,9,12,13,15–18] Parametric images that utilize the slope and intercept parameters to describe the scattered power spectrum have been used by Feleppa *et al.*[12] and Lizzi *et al.*[13] Insana *et al.* created parametric images using estimates of the average scatterer size to describe tissue microstructure.[9]

The advantage in using estimates of the scatterer properties, like the average scatterer size, is that the estimated property may be related to physical microstructures of the tissues. By relating estimated scatterer properties to physical structures, it may be possible to verify the models. Furthermore, if the estimated scatterer properties can be related to real physical structures in tissues, then a new clinical capability presents itself to diagnose tissue disease. If data processing strategies are found that improve the accuracy of estimations, then the utility of parametric imaging for diagnosis of diseased tissues is increased. A few authors have looked at techniques to improve estimates of scatterer properties from backscatter.[19,20] More accurate estimates of scatterer properties have been obtained through optimization of the backscatter measurements and estimation routines. In the work reported herein, a new optimization technique is introduced that increases the accuracy of scatterer property estimations from an attenuating medium. The technique extends the work of previous researchers to increase the accuracy of scatterer property estimations.[20] The new technique uses prior knowledge about the expected SNR of the frequency components in the scattered power spectrum to increase the accuracy of estimation schemes.

Section II explains the theoretical basis for the enhanced estimation technique. The enhanced estimation technique is based on weighting different frequency components used in the estimation according to their expected SNR. Section III discusses simulations and an experiment from a phantom with glass beads. The simulations were constructed to model

[a]Author to whom correspondence should be addressed. Electronic mail: oelze@brl.uiuc.edu

scattering from glass beads and Gaussian scatterers embedded in a tissue-like medium. The phantom experiment was conducted to verify the simulations and the use of the enhanced estimation technique. Section IV applies the enhanced estimation technique to parametric B-mode images of a rat that had developed a spontaneous mammary tumor. The last section includes some concluding remarks about improvement in scattering property estimates achieved by the enhanced estimation technique.

## II. THEORETICAL DESCRIPTION

Average effective scatterer sizes and acoustic concentrations from tissues or other media can be estimated from backscattered RF signals.[3,5,6,21–23] The estimates of scatterer sizes from backscattered RF signals are attractive because they allow the resolving of subwavelength structure in a statistical sense. The methods of estimation assume single scatter theory (no multiple scattering) and examine cases where the scatter is incoherent, i.e., no periodic structures. Relating the frequency-dependent RF signal to models of the tissue microstructure leads to estimates of the scatterer properties. The models describe the scattering through the magnitude and shape of the theoretical power spectrum. A method commonly used to estimate scatterer properties is to minimize the average squared deviation (MASD) between the theoretical power spectrum and the measured power spectrum. The best estimate of the desired scatterer property is the value of the scatterer property that minimizes the squared difference[5,6]

$$\mathrm{MASD}=\min\left\{\frac{1}{B}\sum_{i=1}^{B}(M_i-T_i)^2\right\}, \tag{1}$$

where $B$ is the number of samples in the analysis bandwidth and $M_i$ and $T_i$ are the logarithms of the measured and theoretical power spectra of the scattered RF signal expressed in dB, respectively. Trial and error could be used to find the scatterer properties that give the MASD or more elegant methods like the steepest descent could be used.[24]

Assuming the theory correctly describes the scattering phenomena, then as the SNR increases, the estimation of scattering properties through the MASD is increasingly accurate. As the SNR decreases, the MASD gives less accurate estimates of the scattering properties.[20] Particular frequency components in the analysis bandwidth will have a larger SNR than other frequency components.

Several factors introduce more noise into the measurement thereby decreasing the SNR for particular frequency components. Two factors that determine lower SNR at particular frequencies are the bandwidth and amplitude of the excitation-pulse power spectral shape.[20] The scattered power is proportional to the spectral power of the initial excitation pulse. Less power in the excitation pulse means smaller SNR in the scattered signal, especially at frequency components with little magnitude in the excitation-pulse power spectrum ($-6$ dB bandwidth edges assuming a Gaussian spectrum). Attenuation has a dramatic effect on the estimation of scattering properties by reducing signal and decreasing the SNR in the measurement. Typically, attenuation increases with increasing frequency so that the attenuation reduces the SNR at higher frequencies more than at lower frequencies. A third factor that causes low SNR is the magnitude of the scattering power itself. Particular frequencies in the scattered power spectrum are scattered with different magnitudes according to the size, shape and makeup of the scattering particles.[3,5,6] Frequencies that are scattered with a low magnitude contribute to smaller SNR than frequencies scattered with large magnitude. Figure 1 compares a theoretical and measured scattered power spectrum (form factor) from a collection of randomly spaced glass beads of known size versus different $ka$ values for a signal with minimal attenuation losses.[5] The $ka$ value represents the acoustic wave number, $k$, times the average glass bead radius, $a$. The spectra show that different frequency components ($ka$ values) scatter with different magnitudes. Inherent in the measured spectrum is a level of noise. A comparison of the two spectra shows that the ratio of noise to scattering magnitude is greater for certain frequencies than others, namely the larger frequencies.

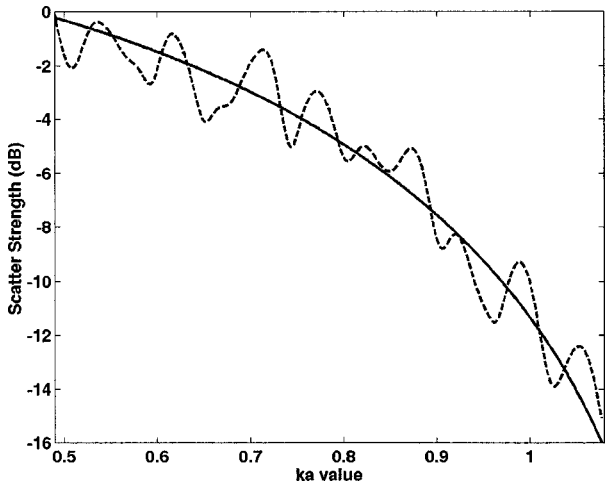


FIG. 1. Comparison of the theoretical and measured backscatter spectra (form factor) from a collection of randomly spaced glass beads of diameter 80 $\mu$m; —, theoretical form factor; ---, measured form factor.

The ability of the MASD to estimate scatterer properties is related to the SNR of the backscattered signals. The more noise there is in the backscattered signal (measured power spectrum) the less accurate the estimates of scatterer properties. Because particular frequency components have different SNRs, those frequency components with larger SNR increase the accuracy of the estimates while the frequency components with smaller SNR decrease the accuracy of scatterer property estimates. By weighting the frequency components in the analysis bandwidth that have larger SNR more than the frequency components that have smaller SNR, improved accuracy in scatterer property estimations can be obtained.[20]

Consider a backscattered RF time signal gated from a region of randomly spaced scatterers

$$x(t)=p(t)*s(t)+n(t), \tag{2}$$

where $p(t)$ is the impulse response of the system (including effects of diffraction and attenuation), $s(t)$ describes the tissue scattering, and $n(t)$ represents the random noise. The noise, $n(t)$, is modeled as a zero-mean Gaussian white noise coming from electronic noise in the system. The measured power spectrum is given by

$$W'_{\text{meas}}(f)=|X(f)|^2=|P(f)|^2|S(f)|^2+|N'(f)|^2, \tag{3}$$

where $|S(f)|^2$ is the power spectrum of the scatterers determined by the size and shape of the scatterers in the medium,[10] $|P(f)|^2$ is the power spectrum of the impulse response, and $|N'(f)|^2$ is the noise contribution to the power spectrum from the electronic noise in the system and from noise related to the random scatterer spacings.[25] If measurements are taken in the depth of focus of the transducer then the power spectrum of the impulse response can be approximated as

$$|P(f)|^2 \approx W_{\text{ref}}(f)A^{-1}(f), \tag{4}$$

where $W_{\text{ref}}(f)$ represents the power spectrum of the excitation pulse and $A^{-1}(f)$ represents the frequency-dependent attenuation loss over the gated length. The function $A(f)$ would represent an attenuation–compensation function. The power spectrum of the excitation pulse is approximated by a calibration (reference) spectrum that is found by measuring the pulse from a planar reflector of known reflectivity located at the same distance from the source to the gated signal.[5,6,26,27] Because the measurements are taken in the depth of focus of the transducer, diffraction effects are considered minimal.

The normalized power spectrum is found by dividing by $W_{\text{ref}}(f)$ and correcting for the attenuation losses with the attenuation–compensation function[6]

$$W_{\text{meas}}(f)=W'_{\text{meas}}(f)\frac{A(f)}{W_{\text{ref}}(f)} \tag{5}$$

giving

$$W_{\text{meas}}(f)=|S(f)|^2+\frac{|N'(f)|^2}{W_{\text{ref}}(f)}A(f)=|S(f)|^2+|N''(f)|^2. \tag{6}$$

Letting

$$M(f_i)=10\log W_{\text{meas}}(f_i) \tag{7}$$

and

$$T(f_i)=10\log|S_T(f_i)|^2 \tag{8}$$

according to Eq. (1) where $S_T(f_i)$ is the theoretical power spectrum, then

$$\text{MASD}=\min\left\{\frac{1}{B}\sum_{i=1}^{B}\left(10\log[|S(f_i)|^2+|N''(f_i)|^2]-10\log|S_T(f_i)|^2)^2\right\}. \tag{9}$$

If the theory correctly describes the scatter then

$$|S_T(f_i)|^2=|S(f_i)|^2. \tag{10}$$

Insertion of Eq. (10) into Eq. (9) yields

$$\text{MASD}=\min\left\{\frac{1}{B}\sum_{i=1}^{B}\left(10\log[|S_T(f_i)|^2+|N''(f_i)|^2]-10\log|S_T(f_i)|^2)^2\right\}. \tag{11}$$

Simplifying Eq. (11) and using the notation $|S_T(f_i)|^2=S_i$ and $|N''(f_i)|^2=N''_i$ gives

$$\text{MASD}=\min\left\{\frac{1}{B}\sum_{i=1}^{B}\left(10\log\left[1+\frac{N''_i}{S_i}\right]\right)^2\right\}. \tag{12}$$

Equation (12) is minimized and the best estimates are made when Eq. (10) holds and the noise is zero (MASD=0). The smallest possible value for the MASD occurs when the summation over the entire analysis bandwidth is zero. When the noise is not zero, another value for $S_T(f_i)$ may exist that does not yield the most accurate estimates of the true scatterer properties but minimizes the average squared deviation. In any real situation, the noise is not zero and the accuracy of the estimates is reduced by the level of noise. In order to get the best estimates from the MASD, Eq. (10) must hold and the noise effects seen in Eq. (12) must be minimized.

To a limited degree, weighting different frequency components based on their expected SNR will reduce the noise effects on the estimates. Defining the SNR according to[19]

$$\text{SNR}=10\log\frac{|S(f_i)|^2}{|N''(f_i)|^2} \tag{13}$$

then as long as the SNR$\geqslant$0, $N''_i/S_i\leqslant 1$ and the term in parenthesis in Eq. (12) can be expanded into a series as

$$\text{MASD}=\min\left\{\frac{1}{B}\sum_{i=1}^{B}\left(\left[\frac{N''_i}{S_i}-\frac{1}{2}\left(\frac{N''_i}{S_i}\right)^2+\frac{1}{3}\left(\frac{N''_i}{S_i}\right)^3-\cdots\right]10\log e\right)^2\right\}. \tag{14}$$

If the $N''_i/S_i\leqslant 1$, then the first term contributes most to the MASD and

$$\text{MASD}\approx\frac{18.8}{B}\sum_{i=1}^{B}\left(\frac{N''_i}{S_i}\right)^2(1-\epsilon)^2, \tag{15}$$

where $\epsilon$ represents some small value. If the frequency dependence of $N''_i/S_i$ can be deduced, then a weighting function can be constructed that reduces the effect of the first term on the estimation scheme.

Let $H_i^2$ be the weighting function that minimizes the effect of the noise on the estimation of scatterer properties through the MASD. The weighting function is implemented into the MASD by

$$\text{MASD}\approx\frac{18.8}{B}\sum_{i=1}^{B}\left(\frac{N''_i}{S_i}\right)^2(1-\epsilon)^2H_i^2. \tag{16}$$

The form of $H_i^2$ depends on the frequency dependence of the ratio $N''_i/S_i$. From the definition of $N''_i$ in Eq. (6)

$$N''_i=N'_i\frac{A(f_i)}{W_{\text{ref}}(f_i)}. \tag{17}$$

Equation (17) shows that the noise function, $N''_i$, and hence $N''_i/S_i$ increases as the attenuation coefficient and propagation distance increases, i.e., $A(f)$ gets larger. Furthermore, dividing the noise by the calibration spectrum, $W_{\text{ref}}(f_i)$, increases the overall magnitude of $N''_i/S_i$ at the edges of the excitation pulse bandwidth, assuming a typical Gaussian-

type bandwidth. At frequency components where the scattering power, $S_i$, is smaller, $N_i''/S_i$ will also be larger. The attenuation–compensation function and calibration spectrum are known and the scattering power can be approximated. Defining

$$\Omega_i = \frac{A(f_i)}{S_i \cdot W_{\text{ref}}(f_i)}, \tag{18}$$

then

$$\text{MASD} \approx \frac{18.8}{B} \sum_{i=1}^{B} N_i'^2 \Omega_i^2 (1-\epsilon)^2 H_i^2. \tag{19}$$

The factor $\Omega_i$ can be defined for each frequency component but the noise factor $N_i'$ and the value of $\epsilon$ cannot be explicitly determined. The factor $\Omega_i$ acts to amplify the noise differently at different frequency components. By defining the weighting function as

$$H_i^2 = \frac{1}{\Omega_i^2} \tag{20}$$

the noise frequency components most amplified by the $\Omega_i$ factor are given less weight in the estimation process. The weighting scheme can be compared to placing a Wiener filter on the original measured spectrum except that the filtering is done on the squared difference between the logarithm of the actual measured spectrum and the theoretical spectrum. No matter what shape the original noise spectrum, $N_i'$, the weighting scheme will give improvement to the accuracy of estimates because the weighting function cancels the amplification of noise by the $\Omega_i$ factor. The solution for $H_i^2$ weights the MASD according to the known attenuation losses, the shape of the excitation pulse and the approximated scattered power spectrum.

## III. SIMULATIONS AND PHANTOM EXPERIMENT

To test the effectiveness of the SNR weighting, simulations were constructed to model scattering from a random, lossy medium. The simulations used different kinds of scatterers of various sizes in media with different attenuation coefficients to examine the ability of the SNR weighting scheme to improve estimation of scatterer properties under different conditions. The attenuation in each of the simulations was chosen to represent what is commonly found in biological tissues. An experiment was performed using backscatter data collected from a real phantom[28] with random scatterers. These data were used to verify the effectiveness of the SNR weighting and the accuracy of the simulations. Estimates of the average scatterer diameter were made from simulations and the phantom measurement with and without the SNR weighting and compared.

Each simulation was constructed by creating a volume matrix with scatterers placed randomly in the matrix. A certain volume of the scatterers corresponding to the beam of the transducer was excited by an acoustic pulse. A wavetrain of backscattered pulses was then created by summing the scattered excitation pulses from each scatterer back at the source aperture. The effects of the medium attenuation were incorporated in propagation of the pulse to and from each scatterer back to the source. Electronic noise was simulated by adding zero-mean Gaussian white noise with standard deviation of $-40$ dB the amplitude of the calibration pulse at the focus. All scattering in the simulations were constructed to take place in the depth of focus of the transducer.

Estimates were made from the backscattered echoes, simulated and measured from the phantom. The ultrasonic bandwidth used for the estimates ranged from 5 to 11 MHz with a center frequency of 8 MHz for the simulations and 8.3 MHz for the phantom experiment. The transducer used in the measurements had an aperture diameter of 12 mm and a focal length of 58 mm. The simulated and measured backscattered RF echoes were digitally sampled at 50 MHz. Each scanned A-line was gated into 4-mm sections using a sliding Hanning window (75% overlap). The average normalized power spectrum was measured for each 4-mm section[6,26,27]

$$W_{\text{meas}}(f) = \frac{R^2}{4M} A(f,L) \sum_{n=1}^{M} \frac{W_n(f)}{W_{\text{ref}}(f)}, \tag{21}$$

where $W_n(f)$ is the measured power spectrum from a single A-line, $A$ is an attenuation–compensation function,[29] $L$ is the gate length (4 mm in the simulations and phantom experiments) and $R$ is the reflection coefficient of the planar reflector used to obtain the reference spectrum, $W_{\text{ref}}(f)$. The average normalized power spectrum is the average of $M$ power spectra from consecutive gated RF time series (A-lines) over a lateral length of 4 mm. The average normalized power spectrum represents the scattering properties from a 4 mm$\times$4 mm box. In a particular box or region of interest (ROI), each consecutive RF time series is assumed to have similar statistical properties so that the average of the spectra reduces noise and anomalous artifacts that may exist in any spectrum measured from a single RF time series. The $M$ power spectra averaged together represent the ensemble of scatterers in the ROI.

The first simulations were modeled as glass beads in agar and the phantom was made from glass beads embedded in agar. The theoretical power spectrum of scattering from glass beads was described using the form factor models.[5,6] The form factor model for glass beads gives a theoretical power spectrum

$$W_{\text{theor}}(f) = C(a_{\text{eff}}, n_z) f^4 F(f, a_{\text{eff}}), \tag{22}$$

where $C$ is a constant with frequency and a function of the average effective radius, $a_{\text{eff}}$, of the scatterers and the average acoustic concentration, $n_z$, of scatterers. The acoustic concentration is defined as the product of the volumetric concentration of scatterers and the average fractional impedance change between the scatterers and surrounding tissues. $F(f, a_{\text{eff}})$ is the form factor describing the frequency dependence of the scattering based on the size, shape and impedance distribution of the average scatterer.[10] Insana and Hall[5] showed that the form factor for spherical shells closely approximated the form factor for glass beads as calculated using the theory of Faran.[21] The form factor for spherical shells (approximating the glass bead form factor) is given by[5]

$$F_{\text{glass}}(f,a) = \left[ j_0\left( \frac{4\pi f a}{c} \right) \right]^2, \tag{23}$$

where $j_0$ represents the spherical Bessel function of order zero and of the first kind, $c$ is the speed of sound in the medium (1540 m/s) and $a$ is the average radius of the glass beads. The form factor for the spherical shell was used to approximate the form factor for glass beads because it has a closed form solution that did not require numerical calculation using the theory of Faran for each trial diameter.[21]

Estimates of the average scatterer size were found through the MASD between the average normalized power spectrum and the theoretical power spectrum. From Eq. (1)

$$\mathrm{MASD}=\min\left(\frac{1}{B}\sum_{i=1}^{B}\left[10\log W_{\mathrm{meas}}(f_i)-10\log|C(a_{\mathrm{eff}},n_z)f_i^4F(a_{\mathrm{eff}},f_i)|\right]^2\right). \tag{24}$$

Letting

$$X_i=10\log[W_{\mathrm{meas}}(f_i)/F(a_{\mathrm{eff}},f_i)f_i^4] \tag{25}$$

and using the fact that the constant $C$ is not a function of frequency and can be seen as an intercept to define

$$\overline{X}=\langle 10\log C(a_{\mathrm{eff}},n_z)\rangle_B=\langle 10\log[W_{\mathrm{meas}}(f)/F(a_{\mathrm{eff}},f)f^4]\rangle_B \tag{26}$$

yields for the MASD[5,6]

$$\mathrm{MASD}=\min\left(\frac{1}{B}\sum_{i=1}^{B}[X_i-\overline{X}]^2\right). \tag{27}$$

The estimate of the average scatterer radius (diameter) is the argument that minimizes Eq. (27).

Implementation of the SNR weighting is given by

$$\mathrm{MASD}=\min\left(\frac{1}{B}\sum_{i=1}^{B}(X_i-\overline{X})^2H_i^2\right), \tag{28}$$

where $H_i^2$ is given by Eq. (20). The weighting function, $H_i^2$, is known only if the approximate scattered power spectrum, $S_i$, is known. The scattered power spectrum is assumed from measurements of the scattering properties in previous ROIs.

In the scattering medium, different regions of interest (ROIs) were selected to examine their scattering properties. In the measurements of the simulations and phantom experiments, the ROIs were selected to be 4 mm×4 mm boxes. The boxes represented gated backscattered signals in the axial direction averaged over a 4 mm length in the lateral direction. The boxes represented 10 half beamwidths (~0.4 mm) in the lateral direction and 20 wavelengths at the center frequency (8 MHz) in the axial direction. Figure 2 gives a representation of the ROI selection in a scattering medium. Each box had a 75% overlap (sliding Hanning window) of the previous ROI box in the axial and lateral directions. Where the boxes overlapped, estimates of scatterer properties were averaged to give regions of 1 mm×1 mm with distinct estimates. The total length of one scan was 1.5 cm in the lateral direction.

Scatterer estimates from regions of shallow propagation depth were assumed to have the best accuracy because less signal loss was introduced by attenuation. The approximate

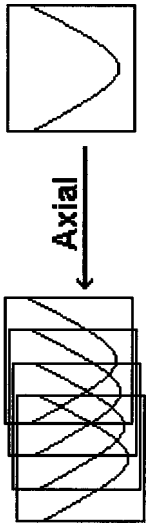


FIG. 2. Representation of the Hanning windowed regions of interest with 75% overlap between regions.

scattered power spectrum, $S_i$, used in the weighting function came from the scattered power spectrum estimated in the previous axial ROI. In the initial ROI of a particular axial line, no weighting with the approximate scattered power spectrum was used because it was assumed that the noise effects were minimal at the shallowest measured depth. By overlapping each ROI with a 75% overlap, the scattering properties from one ROI to the next was assumed to be slowly changing so that the scattered power spectrum used in the weighting function was approximately true.

Figures 3–9 show the estimates of scatterer sizes from simulations and the phantom experiment as the depth increases incrementally by 1 mm (distance between consecutive ROIs) in the scattering media. Figures 3 and 4 show the average estimated scatterer diameters from computer simulations of glass beads in agar. In the simulation for Fig. 3 the sizes of the glass beads are 80 $\mu$m in diameter while the sizes of the glass beads in the simulation for Fig. 4 are 40 $\mu$m in diameter. Both figures show that the estimates made using the SNR weighting provided better estimates of the true scat-

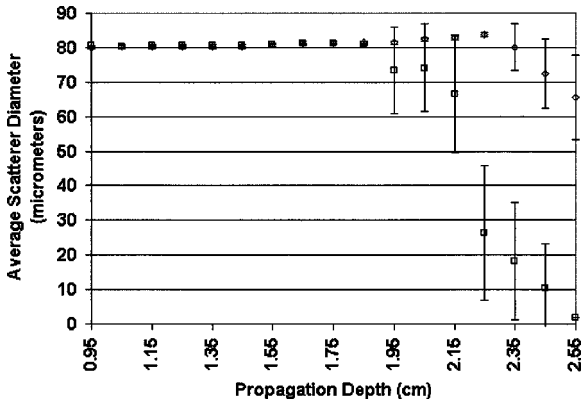


FIG. 3. Estimation of average scatterer diameter from backscattered echoes simulated from an attenuating medium (0.7 dB/MHz/cm) with randomly spaced glass bead scatterers of diameter 80 $\mu$m; □, estimates from simple MASD; ◇, estimates from MASD with SNR weighting. Each estimate is the average 10 estimates from 10 ROIs at the same depth with error bars representing one standard deviation about the average of the 10 estimates.

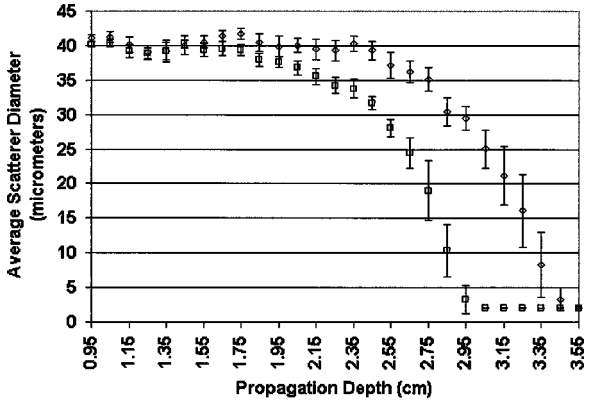


FIG. 4. Estimation of average scatterer diameter from backscattered echoes simulated from an attenuating medium (0.7 dB/MHz/cm) with randomly spaced glass bead scatterers of diameter 40 $\mu$m; □, estimates from simple MASD; ◇, estimates from MASD with SNR weighting. Each estimate is the average 10 estimates from 10 ROIs at the same depth with error bars representing one standard deviation about the average of the 10 estimates.

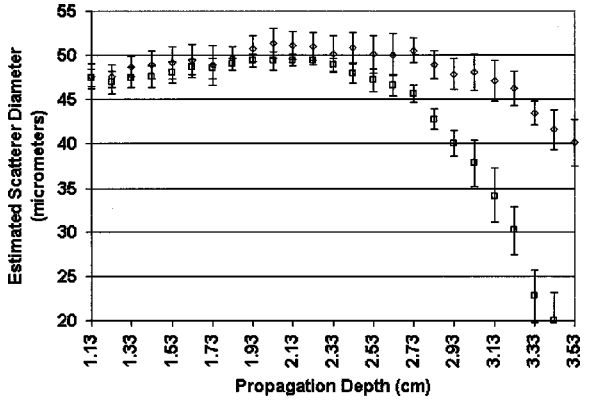


FIG. 6. Estimation of average scatterer diameter from backscattered echoes measured from an agar phantom with attenuation 0.49 dB/MHz/cm and randomly spaced glass bead scatterers of diameter 48±2.5 $\mu$m; □, estimates from simple MASD; ◇, estimates from MASD with SNR weighting. Each estimate is the average 10 estimates from 10 ROIs at the same depth with error bars representing one standard deviation about the average of the 10 estimates.

terer sizes than estimates made without the SNR weighting. Particularly for the larger scatterer sizes (80 $\mu$m) of Fig. 3, the SNR-weighted measurements gave better results. The estimates made with the SNR weighting yielded more accurate results when the total attenuation was larger (SNR was smaller) and appeared to extend the ability to make estimates to a greater propagation depth. For example, in Fig. 3 the ability to estimate the average scatterer diameter within 10% of the actual value from the MASD was extended a half-centimeter in propagation depth using the SNR weighting. In Fig. 4 accurate estimates were extended by more than a half-centimeter in depth using the SNR weighting.

Estimates of scatterer sizes from a phantom embedded with randomly spaced scatterers were also compared with estimates from a simulation. The phantom contained glass beads with diameters of 48±2.5 $\mu$m embedded in agar.[28] The attenuation coefficient of the material was controlled by a concentration of graphite powder and was measured at around 0.49 dB $\mathrm{MHz}^{-1}\,\mathrm{cm}^{-1}$.

A single-element weakly focused transducer was used to scan laterally across the phantom surface. The transducer was moved laterally across the phantom surface by a micropositioning system with step size of 100 $\mu$m between each A-line scan. The transducer had an aperture diameter of 12 mm and a focal length measured at 58 mm from a planar reflector. The center frequency of the transducer was 8.3 MHz with a −6-dB pulse-echo frequency bandwidth of 6 MHz. The analysis bandwidth ranged from 5 to 11 MHz. Figure 10 shows the calibration spectrum measured near the focus of the transducer from a planar surface and the backscattered spectrum from the phantom at the focus. Estimates of scatterer properties were made in the −6-dB pulse-echo depth of focus of the transducer, which ranged from 4.45 cm to 7.45 cm from measurements off a planar reflector.

The transducer was operated in pulse-echo mode through a Panametrics 5800 pulser/receiver (Waltham, MA). The signals were recorded and digitized on an oscilloscope (Lecroy 9354 TM; Chestnut Ridge, NY) that had a dynamic

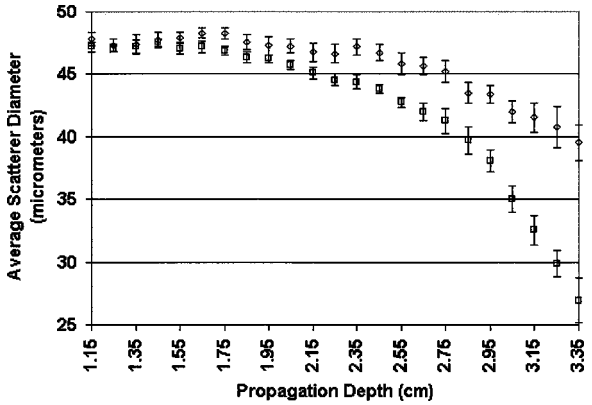


FIG. 5. Estimation of average scatterer diameter from backscattered echoes simulated from an attenuating medium (0.49 dB/MHz/cm) with randomly spaced glass bead scatterers of diameter 48 $\mu$m; □, estimates from simple MASD; ◇, estimates from MASD with SNR weighting. Each estimate is the average 10 estimates from 10 ROIs at the same depth with error bars representing one standard deviation about the average of the 10 estimates.

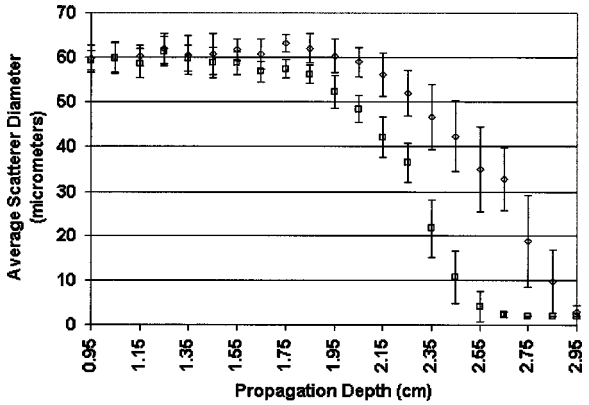


FIG. 7. Estimation of average, effective scatterer diameter from backscattered echoes simulated from an attenuating medium (0.7 dB/MHz/cm) with randomly spaced Gaussian scatterers of effective diameter 60 $\mu$m; □, estimates from simple MASD; ◇, estimates from MASD with SNR weighting. Each estimate is the average 10 estimates from 10 ROIs at the same depth with error bars representing one standard deviation about the average of the 10 estimates.

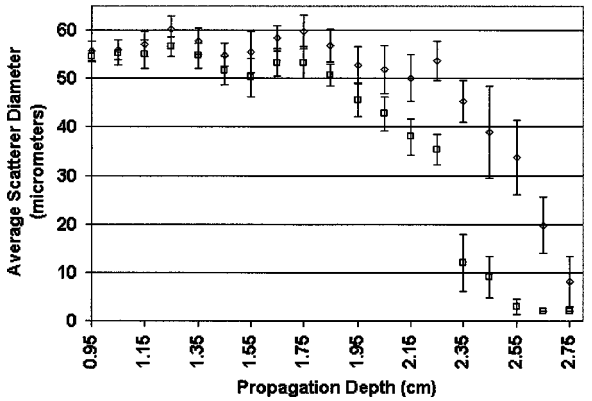


FIG. 8. Estimation of average, effective scatterer diameter from backscattered echoes simulated from an attenuating medium (0.7 dB/MHz/cm) with randomly spaced Gaussian scatterers of effective diameter $60\pm20$ $\mu$m with a Gaussian distribution of scatterer sizes; □, estimates from simple MASD; ◇, estimates from MASD with SNR weighting. Each estimate is the average 10 estimates from 10 ROIs at the same depth with error bars representing one standard deviation about the average of the 10 estimates.

range of 48 dB and downloaded to a PC computer for post-processing. The sampling rate was 50 MHz.

A simulation was also constructed with glass bead scatterers of the same size and concentration and with the same attenuation coefficient as the phantom. Figures 5 and 6 show the results of estimates of the scatterer sizes from the simulation and the phantom measurements, respectively. Comparison of Figs. 5 and 6 shows that the simulation predicted well the improvement achieved using the SNR weighting function in the phantom estimates. Examination of the phantom results and the simulation showed that the ability to estimate the scatterer diameters accurately was increased by almost one centimeter using the SNR weighting for the particular attenuation and glass bead size. In addition, estimates from populations of scatterers with diameters of 40, 48, and 80 $\mu$m were examined to show that SNR weighting gave improvements for estimates of different scatterers sizes relative to acoustic wavelength.

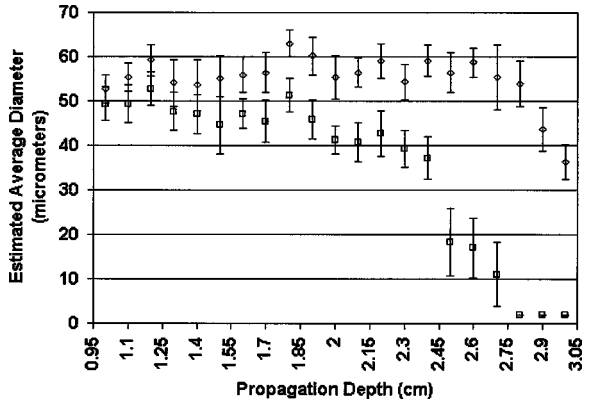


FIG. 9. Estimation of average, effective scatterer diameter from backscattered echoes simulated from an attenuating medium (0.7 dB/MHz/cm) with randomly spaced Gaussian scatterers of average effective diameter 60 $\mu$m with a uniform distribution of scatterer sizes between 40 and 80 $\mu$m; □, estimates from simple MASD; ◇, estimates from MASD with SNR weighting. Each estimate is the average 10 estimates from 10 ROIs at the same depth with error bars representing one standard deviation about the average of the 10 estimates.

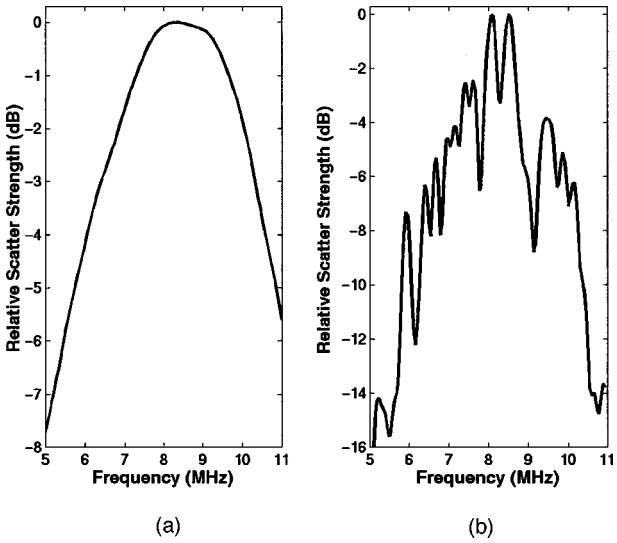


FIG. 10. (a) Example of the calibration spectrum of the ultrasound pulse used in the phantom measurements reflected from a planar surface located near the transducer focus. (b) Example of the measured power spectrum backscattered from the transducer focus in a tissue-mimicking phantom.

A simulation was also constructed using Gaussian scatterers instead of glass beads. Gaussian scatterers are similar to glass beads because they represent spherical particles. Unlike the glass bead, however, the Gaussian scatterer represents an impedance change that varies continuously with the surrounding medium. A glass sphere has an abrupt change in impedance between the surrounding medium and the particle and, hence, a definite diameter. Instead of having a definite diameter, the Gaussian scatterer has an effective diameter. The effective diameter represents the width of the $-6$-dB edge of the Gaussian function describing the impedance distribution of the scatterer.[3]

Gaussian scatterers are described by the form factor[5]

$$F_{\text{Gauss}}(f)=e^{-0.75(2\pi f/c)^2 a_{\text{eff}}^2}, \tag{29}$$

where the constant in the exponential is used to normalize the effective radius to the $-6$-dB edge of the Gaussian function. Gaussian scatterers have been used to describe the scattering from many soft tissues.[1,3–6,10] For the theoretical power spectrum using the Gaussian form factor, the MASD can be simplified. Inserting Eq. (29) into Eq. (22) gives for the theoretical log power spectrum of Eq. (8),[30]

$$T(f_i)=10\log f_i^4+m(a_{\text{eff}})f_i^2+b(a_{\text{eff}},n_z), \tag{30}$$

where $f_i$ is a particular frequency component in the analysis bandwidth. The last two terms can be thought of as a line ($y=mx+b$) where $x=f_i^2$. The slope parameter, $m$, is a function of the average effective scatterer radius (diameter) and the intercept parameter is a function of the average effective scatterer diameter and acoustic concentration. The MASD, Eq. (1), is then given by

$$\text{MASD}=\min\left\{\frac{1}{B}\sum_{i=1}^{B}\left(10\log W_{\text{meas}}(f_i)-10\log f_i^4 - m(a_{\text{eff}})f^2-b(a_{\text{eff}},n_z)\right)^2\right\}. \tag{31}$$

Letting

$$X_i = 10\log[W_{\text{meas}}(f_i)/f_i^4] - m(a_{\text{eff}})f_i^2 = y_i - m(a_{\text{eff}})f_i^2 \quad (32)$$

and calculating the average intercept

$$\overline{X} = \langle b(a_{\text{eff}}, n_z)\rangle_B = \frac{1}{B}\sum_{i=1}^{B} y_i - m(a_{\text{eff}})f_i^2 \quad (33)$$

then the MASD with the SNR weighting is given by Eq. (28). The MASD is determined when the diameter or the slope parameter, $m$, is found that minimizes the squared difference of Eq. (28). Lizzi *et al.* have estimated scatterer parameters from the measured power spectrum by fitting a line to the measured log power spectrum with $x = f$.[13] Equation (30) shows that the theoretical log power spectrum and, therefore, the measured log power spectrum is not linear. By subtracting $10\log f^4$ from the measured log power spectrum according to Eq. (30) and fitting a line with $x = f^2$, a better fit to the measured log power spectrum can be made.[30]

When using the Gaussian form factor to model the scattering, the slope, $m$, that minimizes the average squared difference of Eq. (28) can be found by taking the derivative of Eq. (28) with respect to $m$ and setting it equal to zero

$$\frac{\partial}{\partial m}\left(\frac{1}{B}\sum_{i=1}^{B}(X_i - \overline{X})^2 H_i^2\right) = 0. \quad (34)$$

Evaluation of Eq. (34) gives

$$\frac{1}{B}\sum_{i=1}^{B}(X_i - \overline{X})H_i^2\left(\frac{\partial X_i}{\partial m} - \frac{\partial \overline{X}}{\partial m}\right) = 0, \quad (35)$$

where

$$\frac{\partial X_i}{\partial m} = -f_i^2 \quad \text{and} \quad \frac{\partial \overline{X}}{\partial m} = -\frac{1}{B}\sum_{i=1}^{B} f_i^2 = -\overline{f^2}. \quad (36)$$

Simplifying Eq. (35) yields

$$\sum_{i=1}^{B}(y_i - m f_i^2 - \overline{y} + m\overline{f^2})H_i^2(-f_i^2 + \overline{f^2}) = 0. \quad (37)$$

Solving for the slope, $m$, gives

$$m(a_{\text{eff}}) = \frac{\Sigma_{i=1}^{B} y_i f_i^2 H_i^2 - \overline{y}\Sigma_{i=1}^{B} f_i^2 H_i^2 - \overline{f^2}\Sigma_{i=1}^{B} y_i H_i^2 + \overline{y}\overline{f^2}\Sigma_{i=1}^{B} H_i^2}{\Sigma_{i=1}^{B}(f_i^2 - \overline{f^2})^2 H_i^2}. \quad (38)$$

The slope value determined by Eq. (38) is the value of the slope that minimizes the squared deviation between the logarithm of the measured and theoretical power spectra. Once the best-fit slope parameter is found, the estimated average scatterer diameter, $D$, is determined by[30]

$$m(a_{\text{eff}}) \approx -60a_{\text{eff}}^2 = -15D^2. \quad (39)$$

A simulation was constructed as with the glass bead simulations except that the backscattered echoes came from a collection of randomly spaced particles that scattered according to the Gaussian form factor. Comparisons were made of average scatterer size estimates with and without the SNR weighting. Figure 7 shows the estimates of average scatterer size with and without the SNR weighting. The estimates of the average effective size of the Gaussian scatterer were more accurate at larger propagation depth with the SNR weighting. Figure 7 shows that using the SNR weighting in the estimation technique improved the accuracy of the scatterer size estimates and extended the depth at which accurate estimates of scatterer size could be made.

Simulations were also run using Gaussian scatterers with a distribution of sizes about some mean size. Figure 7 represents estimates of scatterer sizes from a collection of randomly spaced scatterers of a single size, 60 $\mu$m. Figures 8 and 9 represent estimates of scatterer sizes from populations of scatterers with a distribution of sizes. Figure 8 shows estimates made from scatterers with a mean size of 60 $\mu$m and a Gaussian distribution of sizes about the mean with standard deviation of 20 $\mu$m. Figure 9 shows estimates made from scatterers with a mean size of 60 $\mu$m and a uniform distribution of scatterers between 40 and 80 $\mu$m.

In Figs. 8 and 9 the overall scattering strength (intercept value) for all scatterers was modeled to be the same regardless of size. If the relative impedance difference between the scattering particles and the surrounding tissues were the same for smaller and larger sized particles, the smaller particles would scatter more weakly than the larger sized particles. By forcing the intercept value for scatterers of each size to be equal, the relative impedance difference is increased for the smaller particles and the relative contribution from scatterers of all sizes were equivalent.

Comparison of Figs. 7, 8, and 9 shows that the distributions of scatterers did not detrimentally effect the SNR weighting scheme. The SNR weighting still increased the depth to which accurate estimates could be made. Figure 9 shows an even larger depth increase than for the single sized population of scatterers in Fig. 7. Error bars are similar for Figs. 7 and 8, but error bars from Fig. 9 tend to be slightly larger for both the SNR weighted estimates and unweighted estimates. The larger error bars are expected from the larger number of scatterers with sizes farther from the mean.

In Figs. 3–9 it is observed that as estimates of scatterer sizes are made from increased depth, a larger and larger underestimation of the scatterer sizes is found with and without the MASD. The reason for the underestimation may be due to the shape of the spherical form factors, the noise and attenuation compensation. Figure 11 shows an example of the Gaussian form factor for three different effective diameters. The more negative the slope of the form factor the

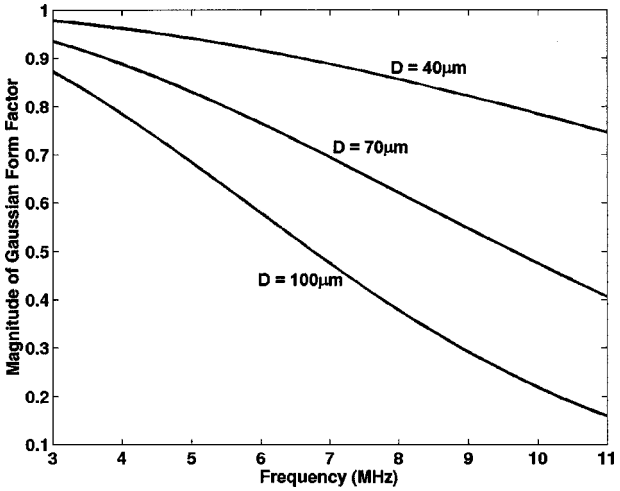


FIG. 11. The magnitude of the Gaussian form factor for spherical scatterers with three different effective diameters, $D$, versus frequency.

larger the scatterer diameter. When the scattered signal is attenuated, the overall SNR is reduced typically more for the higher frequencies than the lower frequencies in the analysis bandwidth. Therefore, when the frequency-dependent attenuation is compensated, the higher frequencies are amplified more than the lower frequencies. The effect of amplifying the noise more at the higher frequencies than the lower frequencies is to make the overall slope appear less negative with frequency. The less negative slope causes the underestimation of the scatterer sizes. To a degree, the SNR weighting scheme accounts for the underestimation effect. However, if the noise is too large relative to the signal, no amount of weighting can draw out the information.

Figures 3–9 also show that as the propagation depth increases and the signal is more attenuated, the error bars on the estimates increase. In the case of the estimates made without the SNR weighting, the error bars increase because the lower SNR decreases the accuracy of the estimates. Similarly, with the SNR weighting, the error bars also increase with increased propagation depth. The error bars are increased because of the lowering of SNR with depth, however, some of the noise effects are mitigated by the SNR weighting scheme. Some of the increase in the error bars with the SNR weighting may also be due to the effective decrease in the analysis bandwidth. If smaller and smaller frequency bandwidth is used to make estimates of the scatterer properties, the variance in the measurements will increase.[19] The SNR weighting scheme will effectively decrease the analysis bandwidth by weighting some frequency components much larger than other components. In comparing the error bars from estimates made with and without the SNR weighting, a significant difference in the size of the error bars with depth was not seen.

## IV. APPLICATION TO PARAMETRIC IMAGING

The SNR weighting was applied to parametric image formation of a solid tumor in a rat.[30] The average scatterer sizes were estimated from the RF signals used to construct parametric B-mode images of the rat and tumor. The experimental protocol was approved by the campus Laboratory Animal Care Advisory Committee and satisfied all campus and National Institutes of Health rules for the humane use of laboratory animals. A Sprague-Dawley rat (Harlan, Indianapolis, IN) that had developed a spontaneous mammary tumor was evaluated. The rat was euthanized with $CO_2$ and the tumor and surrounding area was shaved and depilated. The rat was then placed on a holder in a tank of degassed water at 37 °C for scanning with an ultrasonic transducer.

A single-element weakly focused transducer was used to scan laterally across the tumors and surrounding tissues. The transducer was moved laterally across the chest and tumor by a micropositioning system with step size of 100 $\mu$m between each A-line scan. The transducer had an aperture diameter of 12 mm and a focal length of 58 mm measured from a planar reflector. The center frequency of the transducer was 8.3 MHz with a $-6$-dB pulse-echo frequency bandwidth of 6 MHz. The analysis bandwidth ranged from 5 to 11 MHz. The same transducer was used for the tumor measurement as the phantom measurement. The spectrum of Fig. 10(a) shows the calibration spectrum from the phantom measurement that was also used in the tumor measurement. Estimates of scatterer properties were made in or near the $-6$-dB pulse-echo depth of focus of the transducer.

The transducer was operated in pulse-echo mode through a Panametrics 5800 pulser/receiver (Waltham, MA). The signals were recorded and digitized on an oscilloscope (Lecroy 9354 TM; Chestnut Ridge, NY) that had a dynamic range of 48 dB and downloaded to a PC computer for post-processing. The sampling rate was 50 MHz. The assumed attenuation coefficient in the rat tissues was 0.9 $\mathrm{dB\,MHz^{-1}\,cm^{-1}}$. The large attenuation coefficient value was based on reports of attenuation measurements in the chest walls of rats and mice.[31]

A two-dimensional B-mode image was constructed from the ultrasonic scan lines from the rat. The length of each gated scan line was approximately 3.5 cm. From the 2D B-mode image, ROIs were divided into regions inside and outside the tumor where the B-mode image appeared to be homogeneous (no interfaces or large echoes). The regions scanned and analyzed outside the tumor were intercostal tissues. The tumor was diagnosed as a fibroadenoma following histopathologic evaluation.

Scatterer estimates were made for each ROI using the best-fit line estimation scheme for the Gaussian form factor model, Eq. (38). The backscattered RF signal was gated from each ROI using a sliding Hanning window and the measured power spectrum was calculated according to Eq. (21). The average effective scatterer diameter was estimated from the measured power spectrum for each ROI. The ROIs were 4 mm$\times$4 mm sections from the B-mode image. Each ROI had a 75% overlap (sliding Hanning window) of the previous ROI. By overlapping each ROI by 75% pixels of 1 mm$\times$1 mm were constructed having distinct values for the scatterer size estimate. Each 1 mm$\times$1 mm pixel represented the average scatterer size estimates from one or more overlapping ROIs.

Figure 12 shows a conventional gray-scale B-mode image of the tumor and surrounding tissues in the rat. In Fig. 12, the transducer was located above the image facing down-

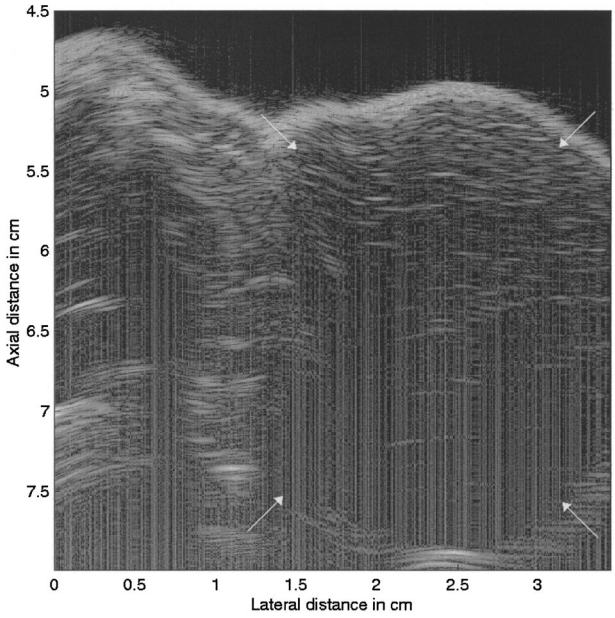


FIG. 12. Conventional, gray-scale B-mode image of rat chest wall and mammary tumor. The tumor is located on the right side of the picture with the white arrows indicating the boundaries of the tumor. Surrounding tissues to the first half-centimeter of depth are intercostal tissues.

wards. The transducer was scanned laterally across the chest from the left to the right side.

Parametric B-mode images of the rat were constructed using the Gaussian form factor and the MASD estimation technique with and without SNR weighting. Figure 13 shows the two parametric images of the rat with tumor. The image on the left shows the parametric image of the rat tissues from size estimates made without the SNR weighting and the image on the right shows the parametric image using the SNR weighting scheme.

A comparison of the two images shows that there exist similarities and important differences between the two images. In the first centimeter of tissue depth, the two images show identical-sized structures. On the left-hand side of each parametric image (axial distance of 5.5 cm and lateral distance of 0 cm) a small area contains estimates of scatterers with very small sizes. The area may represent coherent reflections from some structure in the rat below the chest wall.

As the tissue depth increases, the two images start to show differences. At an axial distance of about 6.5 cm, the parametric image constructed from MASD without SNR weighting begins to give smaller scatterer size estimates within the tumor. At an axial depth of 7 to 7.1 cm, estimates can no longer be made in the tumor (less than the assumed cutoff value of 20 $\mu$m). The parametric image constructed with MASD and the SNR weighting obtains estimates out to bottom edge of the tumor (around 7.7 cm). More of the structure of the tumor and surrounding tissues is seen at a greater propagation depth in the enhanced parametric image than from the image made without SNR weighting. However, it is important to note that in the tumor at 7 cm depth, certain sections appear to give increasingly smaller estimates.

The smaller scatterer size estimates may indicate structure or it may indicate that the MASD with the SNR weighting is beginning to give inaccurate estimates. A limit exists to the gains that can be achieved using the SNR weighting. When the signal is completely lost in the noise, it is impossible to obtain any estimates no matter how the frequency components are weighted.

The parametric images of Fig. 13 show that the overall improvement of the SNR weighting is to extend the ability to make estimates to one-half centimeter and more in propagation depth of the imaged tumor. Determination of the accuracy of the estimates becomes difficult with biological materials since they cannot be characterized in the same detail as phantoms. Furthermore, the exact mechanisms of scattering are not always clearly known. The average effective radius may not be a true average of the scatterer sizes in the tissues but may be a combination of several sized scatterers weighted by the strength of the individual scatterers, i.e., the tissue may hypothetically be made of small scatterers that scatterer strongly and large scatterers that scatterer weakly.

## V. CONCLUSION

A new technique was introduced that gives improved accuracy to estimates of scatterer properties from backscatter echoes in an attenuating media. Previous estimation routines did not take into account the decreased SNR for particular frequency components of the scattered spectrum when the signal propagated through an attenuating medium. The new technique enhanced existing estimation schemes by weighting less the contribution of frequency components that were expected to have smaller SNR than frequency components that were expected to have the largest SNR. Both the simu-

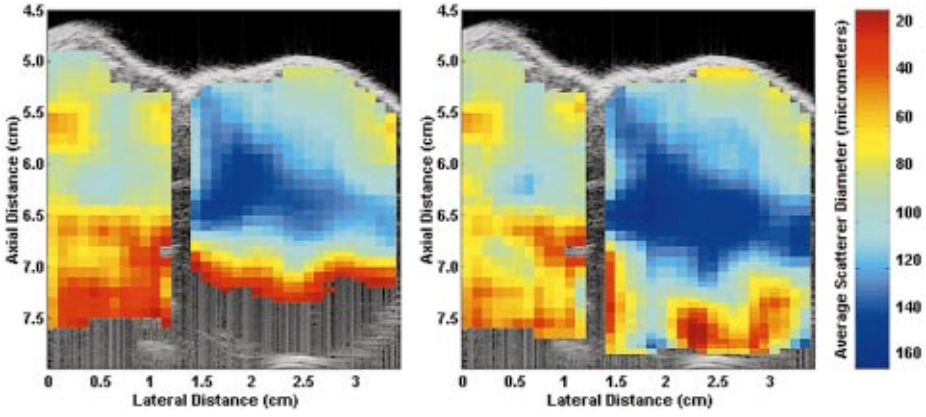


FIG. 13. Parametric B-mode image of rat chest wall and mammary tumor enhanced by average scatterer size estimations using a Gaussian form factor model and MASD without (left) SNR weighting and with (right) SNR weighting.

lations and the phantom experiment showed that the SNR weighting improved the accuracy of scatterer size estimates and extended the ability to obtain estimates to a greater propagation depth. The frequency weighting technique was applied to different kinds of scatterers that are encountered in biological tissues (hard spheres and Gaussian-type scatterers).

The frequency weighting technique was successfully applied to parametric images of spontaneous mammary tumors in rats. The parametric images showed that the SNR weighting technique extended the ability to obtain estimates at a greater propagation depth in the tissues. Furthermore, structure that was not seen without the SNR weighting could be seen with the SNR weighted images. The improvement seen in the parametric images of the rat chest wall and mammary tumor showed that the estimation schemes enhanced with the SNR weighting could aid in increasing the utility of parametric imaging for medical purposes.

## ACKNOWLEDGMENTS

Thanks to James P. Blue and Rita J. Miller, DVM, for their technical assistance. This work was supported by NIH Grants Nos. CA09067 and CA79179.

[1] D. Nicholas, ''Evaluation of backscattering coefficients for excised human tissues: results, interpretation and associated measurements,'' Ultrasound Med. Biol. **8**, 17–28 (1982).
[2] E. J. Feleppa, F. L. Lizzi, D. J. Coleman, and M. M. Yaremko, ''Diagnostic spectrum analysis in ophthalmology: a physical perspective,'' Ultrasound Med. Biol. **12**, 623–631 (1986).
[3] F. L. Lizzi, M. Ostromogilsky, E. J. Feleppa, M. C. Rorke, and M. M. Yaremko, ''Relationship of ultrasonic spectral parameters to features of tissue microstructure,'' IEEE Trans. Ultrason. Ferroelectr. Freq. Control **33**, 319–329 (1986).
[4] D. K. Nassiri and C. R. Hill, ''The use of angular scattering measurements to estimate structural parameters of human and animal tissues,'' J. Acoust. Soc. Am. **87**, 179–192 (1990).
[5] M. F. Insana, R. F. Wagner, D. G. Brown, and T. J. Hall, ''Describing small-scale structure in random media using pulse-echo ultrasound,'' J. Acoust. Soc. Am. **87**, 179–192 (1990).
[6] M. F. Insana and T. J. Hall, ''Parametric ultrasound imaging from backscatter coefficient measurements: image formation and interpretation,'' Ultrason. Imaging **12**, 245–267 (1990).
[7] M. F. Insana, J. G. Wood, and T. J. Hall, ''Identifying acoustic scattering sources in normal renal parenchyma from the anisotropy in acoustic properties,'' Ultrasound Med. Biol. **18**, 587–599 (1992).
[8] K. K. Shung and G. A. Thieme, *Ultrasonic Scattering in Biological Tissues* (CRC Press, Boca Raton, FL, 1993).
[9] M. F. Insana, T. J. Hall, J. G. Wood, and Z-Y. Yan, ''Renal ultrasound using parametric imaging techniques to detect changes in microstructure and function,'' Invest. Radiol. **28**, 720–725 (1993).
[10] M. F. Insana, ''Modeling acoustic backscatter from kidney microstructure using an anisotropic correlation function,'' J. Acoust. Soc. Am. **97**, 649–655 (1995).
[11] T. J. Hall, M. F. Insana, L. A. Harrison, and G. G. Cox, ''Ultrasonic measurement of glomerular diameters in normal adult humans,'' Ultrasound Med. Biol. **22**, 987–997 (1996).
[12] E. J. Feleppa, T. Liu, A. Kalisz, M. C. Shao, N. Fleshner, and V. Reuter, ''Ultrasonic spectral-parameter imaging of the prostate,'' Int. J. Imaging Syst. Technol. **8**, 11–25 (1997).
[13] F. L. Lizzi, M. Astor, T. Liu, C. Deng, D. J. Coleman, and R. H. Silverman, ''Ultrasonic spectrum analysis for tissue assays and therapy evaluation,'' Int. J. Imaging Syst. Technol. **8**, 3–10 (1997).
[14] R. M. Golub, R. E. Parsons, B. Sigel, E. J. Feleppa, J. Justin, H. A. Zaren, M. Rorke, J. Sokil-Melgar, and H. Kimitsuki, ''Differentiation of breast tumors by ultrasonic tissue characterization,'' J. Ultrasound Med. **12**, 601–608 (1993).
[15] K. A. Topp, J. F. Zachary, and W. D. O'Brien, Jr., ''Quantifying B-mode images of *in vivo* rat mammary tumor with frequency dependence of backscatter,'' J. Ultrasound Med. **20**, 605–612 (2001).
[16] S. L. Bridal, P. Fornes, P. Bruneval, and G. Berger, ''Parametric (integrated backscatter and attenuation) images constructed using backscattered radio frequency signals (25–56 MHz) from human aortae *in vitro*,'' Ultrasound Med. Biol. **23**, 215–229 (1997).
[17] J. A. Zagzebski, Z. F. Lu, and L. X. Yao, ''Quantitative ultrasound imaging: *in vitro* results in normal liver,'' Ultrason. Imaging **15**, 335–351 (1983).
[18] R. H. Silverman, R. Folberg, H. C. Boldt, H. O. Lloyd, M. J. Rondeau, M. G. Mehaffey, F. L. Lizzi, and D. J. Coleman, ''Correlation of ultrasound parameter imaging with microcirculatory patterns in uveal melanomas,'' Ultrasound Med. Biol. **23**, 573–581 (1997).
[19] P. Chaturvedi and M. F. Insana, ''Error bounds on ultrasonic scatterer size estimates,'' J. Acoust. Soc. Am. **100**, 392–399 (1996).
[20] P. Chaturvedi and M. F. Insana, ''Bayesian and least squares approaches to ultrasonic scatterer size image formation,'' IEEE Trans. Ultrason. Ferroelectr. Freq. Control **44**, 152–160 (1997).
[21] J. J. Faran, Jr., ''Sound scattering by solid cylinders and spheres,'' J. Acoust. Soc. Am. **23**, 405–418 (1951).
[22] P. M. Morse and K. U. Ingard, *Theoretical Acoustics* (McGraw-Hill, New York, 1968).
[23] A. Ishimaru, *Wave Propagation and Scattering in Random Media* (Academic, New York, 1978).
[24] J. D. Faires and R. L. Burden, *Numerical Methods* (PWS Publishing, Boston, MA, 1993).
[25] K. A. Wear, R. F. Wagner, M. F. Insana, and T. J. Hall, ''Application of autoregressive spectral analysis to cepstral estimation of mean scatterer spacing,'' IEEE Trans. Ultrason. Ferroelectr. Freq. Control **40**, 50–58 (1993).
[26] F. L. Lizzi, M. Greenbaum, E. J. Feleppa, and M. Elbaum, ''Theoretical framework for spectrum analysis in ultrasonic characterization,'' J. Acoust. Soc. Am. **73**, 1366–1373 (1983).
[27] R. A. Sigelmann and J. M. Reid, ''Analysis and measurement of ultrasound backscattering from an ensemble of scatterers excited by sine-wave bursts,'' J. Acoust. Soc. Am. **53**, 1351–1355 (1973).
[28] E. L. Madsen, F. Dong, G. R. Frank, B. S. Garra, K. A. Wear, T. Wislon, J. A. Zagzebski, H. L. Miller, K. Shung, S. H. Wang, E. J. Feleppa, T. Liu, W. D. O'Brien, Jr., K. A. Topp, N. T. Sanghvi, A. V. Zaitsev, T. J. Hall, J. B. Fowlkes, O. D. Kripfgans, and J. G. Miller, ''Interlaboratory comparison of ultrasonic backscatter, attenuation, and speed measurements,'' J. Ultrasound Med. **18**, 615–631 (1999).
[29] M. L. Oelze and W. D. O'Brien, Jr., ''Comparisons of frequency-dependent attenuation-compensation functions for ultrasonic signals backscattered from random media,'' J. Acoust. Soc. Am. **111**, 2308–2319 (2002).
[30] M. L. Oelze, J. F. Zachary, and W. D. O'Brien, Jr., ''Characterization of tissue microstructure using ultrasonic backscatter: Theory and technique optimization using a Gaussian form factor,'' J. Acoust. Soc. Am. **112**, 1202–1211 (2002).
[31] G. A. Teotica, R. J. Miller, L. A. Frizzell, J. F. Zachary, and W. D. O'Brien, Jr., ''Attenuation coefficient estimates of mouse and rat chest wall,'' IEEE Trans. Ultrason. Ferroelectr. Freq. Control **48**, 593–600 (2001).